RESEARCH ARTICLE | SEPTEMBER 07 2022

A highly accurate bound-preserving phase field method for incompressible two-phase flows

Yao Xiao (肖姚); Zhong Zeng (曾忠) ✉; Liangqi Zhang (张良奇) ✉; ... et. al

Physics of Fluids 34, 092103 (2022)
https://doi.org/10.1063/5.0103277

Physics of Fluids ARTICLE scitation.org/journal/phf

A highly accurate bound-preserving phase field method for incompressible two-phase flows

Cite as: Phys. Fluids **34**, 092103 (2022); doi: 10.1063/5.0103277
Submitted: 15 June 2022 · Accepted: 6 August 2022 ·
Published Online: 7 September 2022

Yao Xiao (肖姚),[1] Zhong Zeng (曾忠),[1,a)] Liangqi Zhang (张良奇),[1,a)] Jingzhu Wang (王静竹),[2] Yiwei Wang (王一伟),[2] Hao Liu (刘浩),[3] and Chenguang Huang (黄晨光)[2]

AFFILIATIONS

[1]College of Aerospace Engineering, Chongqing University, Chongqing 400044, People's Republic of China
[2]Key Laboratory for Mechanics in Fluid Solid Coupling Systems, Institute of Mechanics, Chinese Academy of Sciences, Beijing 100190, People's Republic of China
[3]Chongqing Southwest Research Institute for Water Transport Engineering, Chongqing Jiaotong University, Chongqing 400016, People's Republic of China

[a)]**Authors to whom correspondence should be addressed:** zzeng@cqu.edu.cn and zhangliangqi@cqu.edu.cn

ABSTRACT

In this paper, we propose a phase-field-based spectral element method by solving the Navier–Stokes/Cahn–Hilliard equations for incompressible two-phase flows. With the use of the Newton–Raphson method for the Cahn–Hilliard equation and the time-stepping scheme for the Navier–Stokes equation, we construct three constant (time-independent) coefficient matrixes for the solutions of velocity, pressure, and phase variable. Moreover, we invoke the modified bulk free energy density to guarantee the boundness of the solution for the Cahn–Hilliard equation. The above strategies enhanced computation efficiency and accurate capture of the interfacial dynamics. For the canonical tests of diagonal motion of a circle and Zalesak's disk rotation, the lowest relative errors for the interface profile in contrast to the published solutions highlight the high accuracy of the proposed approach. In contrast to our previous work, the present method approximately produces only one tenth relative errors after one rotation cycle but saves 27.2% computation cost. Furthermore, we note that the mobility parameter adopted appears to produce convergent solutions for the phase field but the distribution of the chemical potential remains divergent, which thereby results in diverse coalescence processes in the two merging droplets example. Therefore, a criterion for the choice of the mobility parameter is proposed based on these observations, i.e., the mobility adopted should ensure the convergence solution for the chemical potential. Finally, the rising bubble is presented to verify the proposed method's versatility under large density (1000) and viscosity contrasts (100), and its advantage in efficiency over previous solver is manifested by 44.9% savings in computation cost.

I. INTRODUCTION

There exists a wealth of two-phase flows in both nature and industrial practice, such as inkjet printing, oil extraction processes, and droplet microfluidic systems. Further advancement of these fields necessitates in-depth studies of such flows. Numerical modeling and simulation of immiscible multiphase flows provide easier access to the detailed flow structure and thereby have attracted broad interest over the past 20 years. The major challenge of simulating these problems comes from the tight coupling between the fluid motions and the interfacial dynamics. Currently, numerical strategies for the representation of the interface come in two flavors: the interface tracking method and the interface capturing method. The former approach distributes Lagrangian marker points on the interface and tracks its movements explicitly, such as the front-tracking method,[1,2] the boundary integral method,[2,3] and the immersed boundary method.[4] Alternatively, the interfacial dynamics can be implicitly captured in a purely Eulerian fashion through an auxiliary scalar function such as the volume of fluid (VOF) method,[5,6] level set method,[7,8] and phase field method (PFM),[9,10] which eases the solution of highly deformable interfacial dynamics. These can be further divided into two categories: sharp interface and diffuse interface. In the realm of the sharp interface method, an interface reconstruction procedure is necessary in the VOF method to determine the curvature of the interface tension force,[11] while the level set method suffers from the violation of the mass conservation and a reinitialization procedure is periodically implemented to remedy such deficiency. It is noted that the special numerical treatments would give rise to computational overhead and deteriorate the physical consistency.

Another interface capturing method is the phase-field method (PFM), which belongs to the diffuse interface approach and uses a diffusive layer with fixed thickness to represent the interface. The pioneering idea was conceived by van der Walls in 1894[12] who suggested adding weakly non-local (gradient) terms in the free energy to stabilize the interface in-between the two phase mixture. Later, Cahn and Hilliard (CH)[13–15] extended this approach and formulated the evolution for the phase field variable by accounting for the local energy at the interface. Notably, the phase-field model can be derived from an energy-based variational formalism, which endows the PFM a firm physical basis and allows it to respect the thermodynamic consistency as well as the mass and energy conservation. The theoretical advantages and the ability to describe the complex interface changes has rendered the PFM a robust and growingly popular choice for simulation of multiphase flows.[16–20] Examples include thermocapillary flows,[21,22] evaporation,[23,24] droplet coalescence,[25] and so on. Despite its success in various applications, an efficient, high accuracy, and longtime stable phase-field-based multiphase flow method is still a tough challenge.[26] The fourth order and nonlinear diffusion term of the Cahn–Hilliard equation poses two difficulties for the numerical simulation: (1) the strong discontinuities in solutions and (2) the stringent time step restriction of explicit schemes,[27] which makes the long-time computations hard to converge to physical results. The situation becomes worse for the scenarios with large density and viscosity contrast. In addition, the sufficiently small mesh spacing is necessary to resolve the narrow interface layer in practical computations, which leads to overwhelming computation expense. Therefore, an efficient and accurate solution for the Navier–Stokes/Cahn–Hilliard equations remains a long-lasting topic of active research,[28] and a high-order method has proved feasible to resolve such an issue. Shen *et al.*[16,29] explicitly pointed out that compared with common second-order methods (such as the finite difference method), the spectral method with the exponential convergence rate can effectively achieve computational savings with less grid points under the same accuracy request. Furthermore, a pressure stabilization scheme was developed by Shen and Yang[30,31] for two-phase flows with large density contrast. Shi and Li[27] proposed a class of implicit–explicit multistep local discontinuous Galerkin schemes for solving nonlinear Cahn–Hilliard equation. Park *et al.*[32,33] proposed a least squares spectral element method with a time-stepping procedure to the isothermal Navier–Stokes/Cahn–Hilliard system. Manzanero *et al.*[34,35] presented a nodal Discontinuous Galerkin spectral element method for the Cahn–Hilliard equation and developed an entropy-stable incompressible two-phase flow solver. Ma *et al.*[36] put forth a spectral difference-based phase field lattice Boltzmann method (LBM) for incompressible two-phase flows.

Another challenge facing the phase-field-based method is the variation in time of the coefficient matrices of the linear algebraic equations for velocity, pressure, and the phase variable, which roots in the variable density and variable viscosity with respect to the phase variable. Therefore, an update of the coefficient matrices for each time step is necessary for the practical computations and heavily harms the efficiency.[37] Reformulating the coefficient matrix for the linear algebraic equations to remove its dependence on time, an efficient time-stepping scheme was developed by Dong and Shen[37] within the spectral element method framework, and its versatility for large-density-ratios problems and thermal two-phase flows has been well proved.[38]

The third concern is the mobility dependent solution of the PFM, and the evidence for such dependence is rich in the literature. Inamuro[39] found that the coalescence process of the rising bubble is sensitive to the value of the mobility. Huang *et al.*[40] explored the mobility-dependent bifurcations in a capillarity-driven two-phase fluid system by the lattice Boltzmann model. Chen *et al.*[41] examined the mobility influence on the two merging bubbles problem, and they observed that the mobility could significantly affect the coalescence process. Despite the consensus on the influence of mobility, there still lacks deterministic criteria for a proper choice of the mobility parameter, which hampers further application in practice. Several researchers are concerned about this issue and proposed criteria for the proper choice of mobility. Jacqmin[42] found, by some theoretical and numerical analysis, that mobility M_0 should be bounded between $O(Cn^2)$ and $O(Cn)$ to ensure that the diffuse interface approximation can approach its shape interface limit. Here, $Cn = \varepsilon/L$, is the non-dimensional thickness of the interface, where ε is the interface width and L is the characteristic length. Khatavkar *et al.*[43] approached the problem on numerical grounds, proposing the scaling relation $M_0 \propto 1/Cn$. Magaletti *et al.*[44] correlated the mobility with the characteristic velocity, interface width, and surface tension σ as $M_0 \cong \varepsilon^2 U/L$ by a formal asymptotic analysis. Recently, Sharma *et al.*[45] extended such correlation and proposed to determine the mobility value adaptively based on the local interface thickness.

In this work, we address the above concerns by proposing an alternative phase-field-based spectral element method. The Newton–Raphson method is adopted to resolve the Cahn–Hilliard equation, and the time-stepping scheme[37] is used for the Navier–Stokes equations. In this way, coefficient matrixes of the linear algebraic equations for velocity, pressure, and phase variable become time-independent and can be pre-computed during the pre-processing step. In addition, we replace the original double well potential function with a modified bulk free energy density to preserve the boundness of the solution of the Cahn–Hilliard equation. Therefore, the proposed method imparted both enhanced computation efficiency and high accuracy for interface capture. We present canonical examples to validate the proposed method for two-phase flows, including diagonal motion of a circular interface, Zalesak's disk rotation, single vortex flow, two merging droplets, and bubble rising with large density contrast. The accuracy for interface capture is quantitatively verified by the first three tests, while the last two tests are utilized to prove the robustness and accuracy for complex changes in the interfacial topology under large fluid property contrast. Finally, through the two merging droplets example, we come up with a criterion for the appropriate choice of the mobility parameter for the present method and manifest its validity numerically.

II. THEORY AND ALGORITHM

A. Governing equations for incompressible two-phase flows

The phase field method uses a diffuse layer with thickness ε to represent the phase interface. The present focus is the phase field model governed by the Cahn–Hilliard equation,[46] which employs a phase variable ϕ to label the disparate phases, i.e., $\phi = 1$, and -1 correspond to fluid 1 and fluid 2, respectively. The two fluids connect by a thin smooth transition layer of thickness ε, so the interface of the mixture can be denoted by the zero-level set of phase variable: $\phi = 0$.

The evolution of the phase variable is described by the convection diffusion equation as

$$\frac{\partial \phi}{\partial t} + \mathbf{u} \cdot \nabla \phi = \nabla \cdot (M_0 \nabla \psi), \tag{1}$$

where $\mathbf{u}$ represents the velocity field. M_0 is the mobility, which characterizes the diffusivity in the interfacial region. ψ is the chemical potential, which is determined by the variation of free energy,

$$\psi = \frac{\delta F}{\delta \phi} = f'_{dw}(\phi) - \varepsilon^2 \nabla^2 \phi. \tag{2}$$

The total free energy F reads as[47]

$$F(\phi) = \int_{\Omega} \left(f_{dw}(\phi) + \frac{\varepsilon^2}{2} |\nabla \phi|^2 \right) d\Omega, \tag{3}$$

where Ω is the computational domain. The first term of the above equation represents the bulk free energy density and commonly follows a double-well form $f_{dw}(\phi) = (\phi^2 - 1)^2/4$. According to Caffarelli and Muler,[48] the Cahn–Hilliard equation does not satisfy the maximum principle, which harms the bound-preserving property of its solution. There are two approaches to handle this non-convex term: one is convex splitting method[49] and other is the stabilization method.[29,50,51] Here, we choose the latter one and its unconditional stability requires that the second derivative of $f_{dw}(\phi)$ to be bounded, which cannot be admitted by $f_{dw}(\phi)$ in its original form. Thus, Shen and Yang[29] and Condette *et al.*[52] propose to modify the $f_{dw}(\phi)$ to have a quadratic growth rate for $|\phi| > 1$ as follows:

$$f_{dw}(\phi) = \begin{cases} (\phi - 1)^2, & \phi > 1, \\ \dfrac{(\phi^2 - 1)^2}{4}, & \phi \in [-1, 1], \\ (\phi + 1)^2, & \phi < 1. \end{cases} \tag{4}$$

Then, $\max_{\phi \in \Re} |f''_{dw}(\phi)| \leq 2$ holds theoretically, as proved by Caffarelli and Muler,[48] the maximum norm of the solution for the Cahn–Hilliard equation is bounded, which can thereby guarantee the boundness of the solution for the Cahn–Hilliard equation, and constitutes the important difference between the present method and previous work.[53] In addition, the second term in Eq. (3) stands for the excess free energy in the interfacial region. At the equilibrium state, the analytical profile along the x-axis for a one-dimensional planar interface gives

$$\phi(x) = \tanh\left(\frac{x}{\sqrt{2}\varepsilon} \right). \tag{5}$$

In this work, we assume that the contact angle is 90°. Thus, the boundary conditions for the Cahn–Hilliard equation is given as[37]

$$\mathbf{n}_w \cdot \nabla \phi = 0 \quad \mathbf{n}_w \cdot \nabla \psi = 0. \tag{6}$$

The interfacial force formula proposed by Liu *et al.*[46,54] as follows:

$$\mathbf{f}_\sigma = \frac{3\sqrt{2}}{4} \frac{\sigma}{\varepsilon} \psi \nabla \phi, \tag{7}$$

where σ represents the surface tension between two fluids. Then, we can obtain the whole governing equations for the incompressible two-phase flow as follows:

$$\rho \left(\frac{\partial \mathbf{u}}{\partial t} + \mathbf{u} \cdot \nabla \mathbf{u} \right) = -\nabla p + \nabla \cdot \left[\mu \left(\nabla \mathbf{u} + (\nabla \mathbf{u})^{\mathrm{T}} \right) \right] + \mathbf{f}_\sigma + \rho \mathbf{g}, \tag{8}$$

$$\nabla \cdot \mathbf{u} = 0, \tag{9}$$

$$\begin{cases} \dfrac{\partial \phi}{\partial t} + \mathbf{u} \cdot \nabla \phi = \nabla \cdot (M \nabla \psi), \\ \psi = f'_{dw}(\phi) - \varepsilon^2 \nabla^2 \phi, \end{cases} \tag{10}$$

where $\mathbf{g}$ is the gravity acceleration. The fluid properties, including density ρ and dynamic viscosity μ, are determined by the phase variable as follows:

$$\rho = \frac{\rho_1 + \rho_2}{2} + \frac{\rho_1 - \rho_2}{2} \bar{\phi}, \quad \mu = \frac{\mu_1 + \mu_2}{2} + \frac{\mu_1 - \mu_2}{2} \bar{\phi}, \tag{11}$$

where the auxiliary $\bar{\phi}$ is introduced for large density ratios as follows:

$$\bar{\phi} = \begin{cases} \phi & if\ |\phi| \leq 1, \\ sign(\phi) & if\ |\phi| > 1, \end{cases} \tag{12}$$

B. Phase-field-based spectral element method for two-phase flows

In this section, we propose a spectral element method for two-phase flow by solving Eqs. (9)–(12). The Newton–Raphson method[55] is first employed for the solution of the Cahn–Hilliard equation with one constant coefficient stiffness matrix. Moreover, we use the time-stepping scheme[37,38] to decouple Navier–Stokes equation into two Poisson-type equations and to reformulate another two constant coefficient stiffness matrices for the Navier–Stokes equation. The reformulated constant coefficient stiffness matrices for the phase variable, velocity, and pressure solutions bring considerable savings in computation expense, by circumventing the coefficient matrix update for each iteration within every time step, which lays the difference between the present method and the previous approach in algorithm design.[53] Let ϕ^n, $\mathbf{u}^n$, and p^n denote the phase, velocity, and pressure field at t_n, respectively. To obtain the flow variables at time t_{n+1}, we solve for phase parameter, pressure, and velocity sequentially as follows:

For phase field ϕ^{n+1},

$$\begin{cases} \dfrac{\gamma_0 \phi^{n+1}}{\Delta t} - \nabla \cdot (M \nabla \psi^{n+1}) = \dfrac{\hat{\phi}}{\Delta t} - \mathbf{u}^{*,n+1} \cdot \nabla \phi^{*,n+1}, \\ \varepsilon^2 \nabla^2 \phi^{n+1} + \psi^{n+1} = 2 f'_{dw}(\phi^n) - f'_{dw}(\phi^{n-1}), \end{cases} \tag{13}$$

where the coefficient γ_0 determines the order of the time discretization as Eq. (22).

For pressure p^{n+1},

$$\begin{aligned} &\gamma_0 \tilde{\mathbf{u}}^{n+1} - \frac{\hat{\mathbf{u}}}{\Delta} t + \frac{1}{\rho_0} \nabla p^{n+1} \\ &\quad = -(\mathbf{u}^{*,n+1} \cdot \nabla) \mathbf{u}^{*,n+1} + \left(\frac{1}{\rho_0} - \frac{1}{\rho^{n+1}} \right) \nabla p^{*,n+1} \\ &\quad - \frac{\mu^{n+1}}{\rho^{n+1}} \nabla \times \nabla \times \mathbf{u}^{*,n+1} + \frac{1}{\rho^{n+1}} \nabla \mu^{n+1} \\ &\quad \times \left[\nabla \mathbf{u}^{*,n+1} + (\nabla \mathbf{u}^{*,n+1})^{\mathrm{T}} \right] + \frac{1}{\rho^{n+1}} \mathbf{f}_\sigma + \mathbf{g}, \end{aligned} \tag{14}$$

$$\nabla \cdot \tilde{\mathbf{u}}^{n+1} = 0, \tag{15}$$

$$\mathbf{n}\cdot\tilde{\mathbf{u}}^{n+1}|_\Gamma = \mathbf{n}\cdot\mathbf{w}^{n+1}. \tag{16}$$

For velocity $\mathbf{u}^{n+1}$,

$$\frac{\gamma_0\mathbf{u}^{n+1}}{\Delta t} - \nu_m\nabla^2\mathbf{u}^{n+1} = \frac{\gamma_0\tilde{\mathbf{u}}^{n+1}}{\Delta t} + \nu_m\nabla\times\nabla\times\mathbf{u}^{*,n+1}, \tag{17}$$

where $\frac{\gamma_0\tilde{\mathbf{u}}^{n+1}}{\Delta t}$ is calculated by Eq. (14) as follows:

$$\begin{aligned}\frac{\gamma_0\tilde{\mathbf{u}}^{n+1}}{\Delta t} &= \frac{\hat{\mathbf{u}}}{\Delta}t - \frac{1}{\rho_0}\nabla p^{n+1} - (\mathbf{u}^{*,n+1}\cdot\nabla)\mathbf{u}^{*,n+1}\\ &+\left(\frac{1}{\rho_0}-\frac{1}{\rho^{n+1}}\right)\nabla p^{*,n+1} - \frac{\mu^{n+1}}{\rho^{n+1}}\nabla\times\nabla\times\mathbf{u}^{*,n+1}\\ &+\frac{1}{\rho^{n+1}}\nabla\mu^{n+1}\cdot\left[\nabla\mathbf{u}^{*,n+1}+(\nabla\mathbf{u}^{*,n+1})^{\mathrm{T}}\right] + \frac{1}{\rho^{n+1}}\mathbf{f}_\sigma + \mathbf{g},\end{aligned} \tag{18}$$

$$\mathbf{u}^{*,n+1} = 2\mathbf{u}^n - \mathbf{u}^{n-1}, \tag{19}$$

$$\mathbf{u}^{n+1}|_\Gamma = \mathbf{w}^{n+1}, \tag{20}$$

where Δt is the time step. For stability reasons, the constant parameters ν_m, ρ_0 are chosen by satisfying

$$\nu_m \geq \frac{1}{2}\frac{\max(\mu_1,\mu_2)}{\min(\rho_1,\rho_2)}, \quad \rho_0 = \min(\rho_1,\rho_2).$$

The present scheme features the formulation of the time-independent constant coefficient matrix by augmenting its correction term $\left(\frac{1}{\rho_0}-\frac{1}{\rho^{n+1}}\right)\nabla p^{*,n+1}$ in Eq. (14) and by bringing $\nu_m\nabla^2\mathbf{u}^{n+1}$ and its correction term $\nu_m\nabla\times\nabla\times\mathbf{u}^{*,n+1}$ in Eq. (17).[37,56,57] We use χ a generic variable to represents $\mathbf{u}$ and ϕ. $\chi^{*,n+1}$ represents a Jth order explicit approximation of χ^{n+1} as follows:

$$\chi^{*,n+1} = \begin{cases}\chi^n & \text{if J} = 1,\\ 2\chi^n - \chi^{n-1} & \text{if J} = 2.\end{cases} \tag{21}$$

where J denotes the order of temporal accuracy. The expression $(\gamma_0\tilde{\chi}^{n+1}-\hat{\chi})/\Delta t$ represents a discretization of $\frac{\partial\chi}{\partial t}$ at time step $(n+1)$ with the Jth order backward differentiation formula with

$$\gamma_0 = \begin{cases}1 & \text{if J} = 1,\\ \frac{3}{2} & \text{if J} = 2.\end{cases} \quad \hat{\chi} = \begin{cases}\chi^n & \text{if J} = 1,\\ 2\chi^n - \frac{1}{2}\chi^{n-1} & \text{if J} = 2.\end{cases} \tag{22}$$

Next, we provide the details for the algorithmic development in the context of the spectral element method. First of all, we solve the phase field equation with the Newton–Raphson method.[55,58] Take the L^2-inner product of Eq. (13) with test functions h and ζ for ϕ and ψ, respectively, in the computational domain Ω. We obtain the weak form of Eq. (13),

$$\begin{cases}\displaystyle\int_\Omega\left(\frac{\gamma_0\phi^{n+1}}{\Delta t} + \mathbf{u}^{*,n+1}\cdot\nabla\phi^{n+1}\right)h\mathrm{d}\Omega + \int_\Omega M\nabla\psi^{n+1}\cdot\nabla h\mathrm{d}\Omega\\ \quad\displaystyle= \int_\Omega\frac{\hat{\phi}}{\Delta t}h\mathrm{d}\Omega - \int_\Omega(\mathbf{u}^{*,n+1}\cdot\nabla\phi^{n+1})h\mathrm{d}\Omega,\\ \displaystyle\int_\Omega\varepsilon^2\nabla\phi^{n+1}\cdot\nabla\zeta\mathrm{d}\Omega - \int_\Omega\psi^{n+1}\zeta\mathrm{d}\Omega\\ \quad\displaystyle= -\int_\Omega 2f'_{dw}(\phi^n)\zeta\mathrm{d}\Omega + \int_\Omega f'_{dw}(\phi^{n-1})\zeta\mathrm{d}\Omega.\end{cases} \tag{23}$$

The residual vector of the above equation in Newton–Raphson method can be expressed as

$$\begin{aligned}R_1 &= \int_\Omega\left(\frac{\gamma_0\phi^{n+1}}{\Delta t} + \mathbf{u}^{*,n+1}\cdot\nabla\phi^{n+1}\right)h\mathrm{d}\Omega\\ &+\int_\Omega M\nabla\psi^{n+1}\cdot\nabla h\mathrm{d}\Omega - \int_\Omega\frac{\hat{\phi}}{\Delta t}h\mathrm{d}\Omega\\ &+\int_\Omega(\mathbf{u}^{*,n+1}\cdot\nabla\phi^{n+1})h\mathrm{d}\Omega,\end{aligned} \tag{24}$$

$$\begin{aligned}R_2 &= \int_\Omega\varepsilon^2\nabla\phi^{n+1}\cdot\nabla\zeta\mathrm{d}\Omega - \int_\Omega\psi^{n+1}\zeta\mathrm{d}\Omega + \int_\Omega 2f'_{dw}(\phi^n)\zeta\mathrm{d}\Omega\\ &-\int_\Omega f'_{dw}(\phi^{n-1})\zeta\mathrm{d}\Omega,\end{aligned} \tag{25}$$

and the Jacobian matrix becomes a constant matrix and is defined as

$$\mathbf{J} = \begin{pmatrix}\frac{\partial R_1}{\partial\phi^{n+1}} & \frac{\partial R_1}{\partial\psi^{n+1}}\\ \frac{\partial R_2}{\partial\phi^{n+1}} & \frac{\partial R_2}{\partial\psi^{n+1}}\end{pmatrix}, \tag{26}$$

where

$$\frac{\partial R_1}{\partial\phi^{n+1}} = \int_\Omega\frac{\gamma_0}{\Delta t}h\mathrm{d}\Omega, \tag{27}$$

$$\frac{\partial R_1}{\partial\psi^{n+1}} = \int_\Omega M\nabla\psi^{n+1}\cdot\nabla h\mathrm{d}\Omega, \tag{28}$$

$$\frac{\partial R_2}{\partial\phi^{n+1}} = \int_\Omega\varepsilon^2\nabla\phi^{n+1}\cdot\nabla\zeta\mathrm{d}\Omega, \tag{29}$$

$$\frac{\partial R_2}{\partial\psi^{n+1}} = -\int_\Omega\psi^{n+1}\zeta\mathrm{d}\Omega. \tag{30}$$

After formulating the residuals and Jacobian matrix, we obtain a set of nonlinear equations as follows:

$$[J]\{d\delta\} = \{R^G\}, \tag{31}$$

where $R^G = (R_1, R_2)^T$ and $d\delta = (d\phi_1, d\phi_2, \ldots, d\phi_N, d\psi_1, d\psi_2, \ldots d\psi_N)^T$ and N is the total number of mesh nodes. As the left-hand

Jacobian matrix $\mathbf{J}$ is a constant matrix, it forms only once before the computation and remains unchanged thereafter. For the remaining iterations, the residual vector R^G is reevaluated and Eq. (31) is then solved again to update the phase variable as $\delta^{n+1} = \delta^n + d\delta$. This Newton–Raphson iteration procedure continues until the norm-2 of ϕ^n and ϕ^{n+1} reach the convergence criteria (error $= 1 \times 10^{-6}$) or a number of iterations reach the maximum.

With the determined phase field ϕ^{n+1} and chemical potential ψ^{n+1}, we can update ρ, μ by Eq. (11). With the aim of solving the pressure and velocity, we set

$$G_p = \frac{\hat{\mathbf{u}}}{\Delta}t - (\mathbf{u}^{*,n+1}\cdot\nabla)\mathbf{u}^{*,n+1} + \left(\frac{1}{\rho_0} - \frac{1}{\rho^{n+1}}\right)\nabla p^{*,n+1} + \frac{1}{\rho^{n+1}}\nabla\mu^{n+1}\cdot\left[\nabla\mathbf{u}^{*,n+1} + (\nabla\mathbf{u}^{*,n+1})^{\mathrm{T}}\right] + \frac{1}{\rho^{n+1}}\mathbf{f}_\sigma + \mathbf{g}. \tag{32}$$

Let us define vorticity as $\boldsymbol{\omega} = \nabla\times\mathbf{u}$. Taking the L^2-inner product of Eq. (14) with ∇h produces the Poisson equation for the weak form of pressure p^{n+1},

$$\int_\Omega \nabla p^{n+1}\cdot\nabla h\,\mathrm{d}\Omega = \rho_0\int_\Omega\left[\mathbf{G} + \nabla\left(\frac{\mu^{n+1}}{\rho^{n+1}}\right)\times\omega^{*,n+1}\right]\times\nabla h\,\mathrm{d}\Omega - \rho_0\int_\Gamma\frac{\mu^{n+1}}{\rho^{n+1}}\mathbf{n}\times\boldsymbol{\omega}^{*,n+1}\cdot\nabla h d\Gamma - \frac{\gamma_0\rho_0}{\Delta t}\int_\Gamma\mathbf{n}\cdot\mathbf{w}^{n+1}h d\Gamma,\quad \forall \mathrm{q}\in H^1(\Omega), \tag{33}$$

where

$$\frac{\mu^{n+1}}{\rho^{n+1}}\nabla\times\boldsymbol{\omega}\cdot\nabla h = \nabla\cdot\left(\frac{\mu}{\rho}\boldsymbol{\omega}\times\nabla h\right) - \nabla\left(\frac{\mu}{\rho}\right)\times\boldsymbol{\omega}^{*,n+1}\cdot\nabla h. \tag{34}$$

Referring to Eqs. (17)–(20), we set

$$\mathbf{G}_u = \mathbf{g} + \frac{\hat{\mathbf{u}}}{\Delta}t + \frac{1}{\rho^{n+1}}\mathbf{f}_\sigma + \frac{1}{\rho^{n+1}}\nabla\mu^{n+1}\cdot\left[\nabla\mathbf{u}^{*,n+1} + (\nabla\mathbf{u}^{*,n+1})^{\mathrm{T}}\right] + \left(\frac{1}{\rho_0} - \frac{1}{\rho^{n+1}}\right)\nabla p^{*,n+1} - (\mathbf{u}^{*,n+1}\cdot\nabla)\mathbf{u}^{*,n+1} + \nabla\left(\frac{\mu^{n+1}}{\rho^{n+1}}\right)\times\boldsymbol{\omega}^{*,n+1} \tag{35}$$

and obtain the weak form of the velocity equation,

$$\frac{\gamma_0}{\nu_m\Delta t}\int_\Omega\mathbf{u}^{n+1}h\mathrm{d}\Omega + \int_\Omega\nabla h\cdot\nabla\mathbf{u}^{n+1}\mathrm{d}\Omega = \frac{1}{\nu_m}\int_\Omega h\left(\mathbf{G} - \frac{1}{\rho_0}\nabla p^{n+1}\right)\mathrm{d}\Omega - \frac{1}{\nu_m}\int_\Omega\left(\frac{\mu^{n+1}}{\rho^{n+1}} - \nu_m\right)\boldsymbol{\omega}^{*,n+1}\times\nabla h\mathrm{d}\Omega - \frac{1}{\nu_m}\int_\Gamma\left(\frac{\mu^{n+1}}{\rho^{n+1}} - \nu_m\right)\mathbf{n}\times\boldsymbol{\omega}^{*,n+1}h\mathrm{d}\Gamma,\quad \forall h\in H_0^1(\Omega). \tag{36}$$

The overall solution procedure can be summarized from the above derivations as follows:

(1) Given $(\mathbf{u}^n, p^n, \phi^n)$, solve Eq. (31) for phase variable ϕ^{n+1} and potential chemical ψ^{n+1} after the norm-2 of ϕ^n and ϕ^{n+1} reach the convergence criteria (1×10^{-6}) or a number of iterations reach the maximum.
(2) Compute the density ρ^{n+1} and dynamic viscosity μ^{n+1} by Eqs. (11) and (12).
(3) Obtain the surface tension $\mathbf{f}_\sigma$ by Eq. (7) with ϕ^{n+1} and ψ^{n+1}.
(4) Solve Eq. (33) for pressure p^{n+1} with ρ^{n+1}, μ^{n+1} and $\mathbf{f}_\sigma$.
(5) Solve Eq. (36) for velocity $\mathbf{u}^{n+1}$ with ρ^{n+1}, μ^{n+1}, $\mathbf{f}_\sigma$ and ∇p^{n+1}.

Summarily, the present two-phase flow solver is built by resolving the Cahn–Hilliard equation with Newton–Raphson iteration and then computing the flow field through the solution of the pressure Poisson in Eq. (33) and the velocity Helmholtz Eq. (36). The Legendre spectral element method[53,59] is adopted for the spatial discretization in this work.

III. BENCHMARK TESTS

In this section, several canonical two-phase flow examples, including diagonal motion of a circular interface,[60–62] Zalesak's disk rotation,[63] and single vortex flow,[61] are presented. In our simulations, unless otherwise stated, the fourth element order is prescribed for all the elements hereinafter, and see Ref. 53 for detailed analysis of the element order effects. The code is completed by the FORTRAN language without parallelization. The hardware conditions for the present computation are provided as follows:

(1) CPU: Intel(R) Core(TM) i9-9900K CPU at 3.60 GHz
(2) Memory: 64 GB
(3) Disk: KINGSTON SA400S37240G

For quantitative validation, the relative error for the interface profile is defined as

$$E_\phi = \frac{\sum_{\mathbf{x}}|\phi(\mathbf{x}, T_f^n) - \phi(\mathbf{x},0)|}{\sum_{\mathbf{x}}|\phi(\mathbf{x},0)|}, \tag{37}$$

where $\phi(\mathbf{x},0)$ is its initial value and $\phi(\mathbf{x}, T_n)$ is the phase variable distribution after n periodic times $T_f^n = L/U_0$. L and U_0 are the characteristic length and velocity. The dimensionless Peclet number (Pe) is defined as $\mathrm{Pe} = U_0\varepsilon/M_0$.[60] In the following three tests, the periodic boundary conditions are applied at all boundaries.

A. Diagonal motion of a circular interface

The diagonal motion of a circular interface under a constant background velocity field $\mathbf{u} = (U_0, U_0)$ is first considered. Initially, a circle with a radius of R is placed at the center of the computation domain $\Omega = [0, L]\times[0, L]$ as sketched in Fig. 1(a), which is resolved by 625 quadrilateral elements (25 elements in both x- and y-directions). The parameters for this test include L = 100 m, U_0 = 0.02 m/s, ε = 3.0 m, and Pe = 600, which is the same as the setup in Ref. 60. The relative error between the numerical results and the analytical solution admits the following formula:

$$\|\delta\phi\|_2 = \sqrt{\frac{\sum_{\mathbf{x}}\left[\phi(\mathbf{x}, T_f^n) - \phi(\mathbf{x},0)\right]^2}{\sum_{\mathbf{x}}\phi(\mathbf{x},0)^2}}, \tag{38}$$

where $\phi(\mathbf{x}, T_f^n)$ is the phase variable distribution after n periods and $\phi(\mathbf{x},0)$ is the initial value. Figure 2 shows the interface evolution for

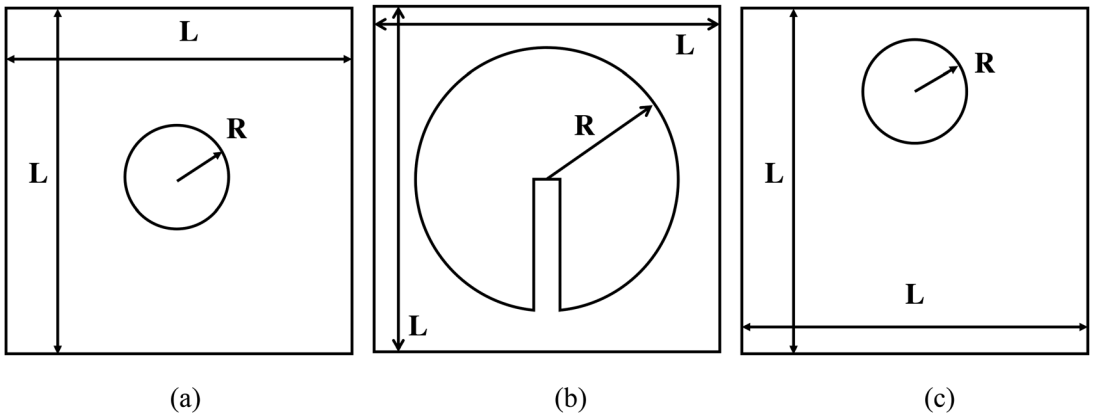

FIG. 1. Initial setup for three benchmark tests: (a) diagonal motion of a circular interface, (b) Zalesak's disk rotation, and (c) single vortex flow.

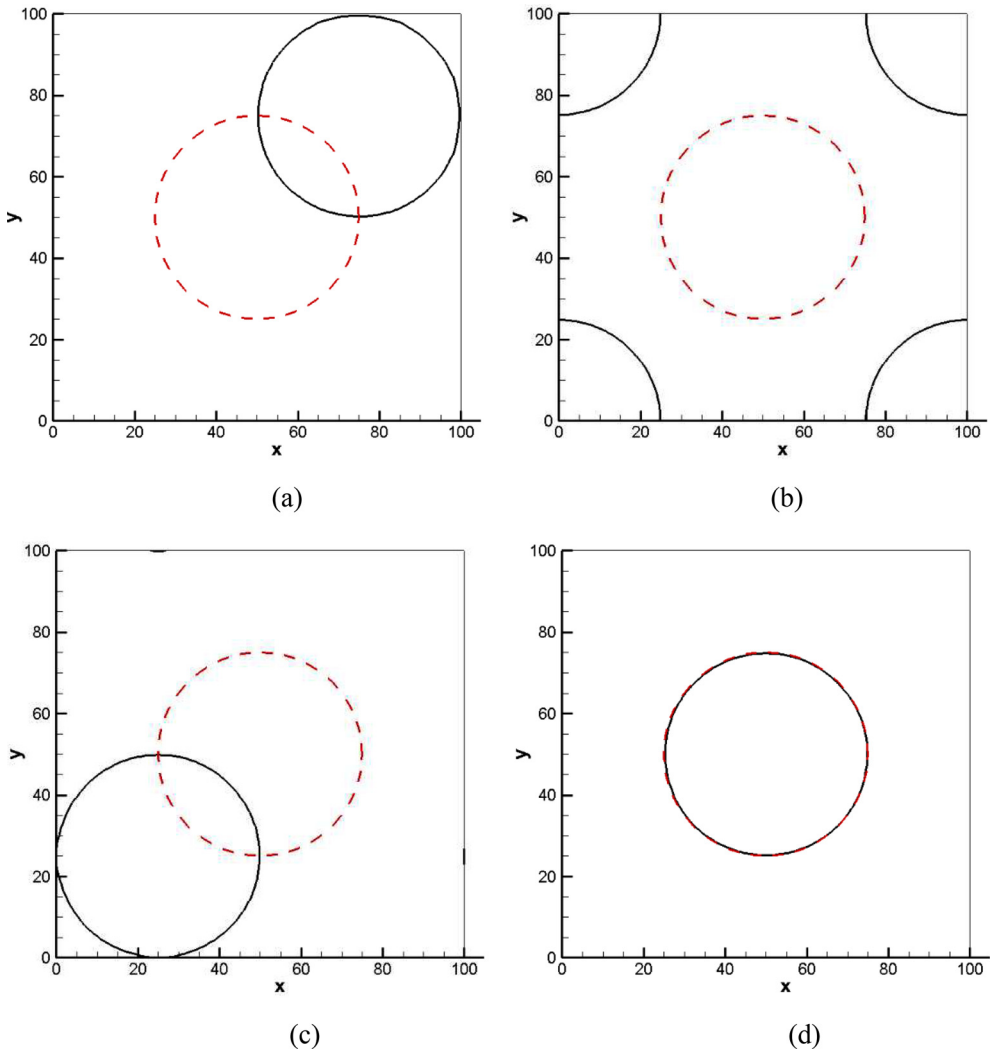

FIG. 2. The phase interface ($\phi = 0$) evolution for the tenth cycle at Pe = 600 (the red dashed line is the initial value, and the black solid line is the numerical solution): (a) t = 9.25 T_f, (b) t = 9.5 T_f, (c) t = 9.75 T_f, and (d) t = 10 T_f.

TABLE I. The relative errors $\|\delta\phi\|_2$ of the present model and literatures[60–62] for the problem of the diagonal motion of a circular interface after ten cycles.

	Liang *et al.*[61] and Zu and He[62]	Present	Geier *et al.*[60]
Relative error	0.1176	0.0377	0.0874

the tenth cycle. The red dashed line and the black solid line, respectively, represent the initial and the numerical interface profile at different times. After ten cycles ($10T_f$), the interface profile from the present method matches well with the theoretical value as demonstrated in Fig. 2(d). We compare the present results with the published work by Zu and He,[62] Liang *et al.*[61] and conservative Allen–Cahn (AC) description by Geier *et al.*[60] in Table I. The relative errors $\|\delta\phi\|_2$ of the present method are apparently much smaller than the reference results.[60–62]

B. Zalesak's disk rotation

Zalesak's disk is widely used for testing the diffusion errors of interface capturing methods.[36,60–62,64–66] It is first introduced by Zalesak[63] to study the accuracy of advection algorithms. Theoretically, the rotating disk will return to its preliminary position after an integer multiple of periods $T_f = 2L/U_0$. A grooved disk with radius R at the start placed in the core of a square with side length L as depicted in Fig. 1(b). The computational domain $\Omega = [0, L] \times [0, L]$ is covered by 2500 quadrilateral elements (50 elements in both x- and y-directions). The parameter setup for the present test is given as $L = 200$ m, $\varepsilon = 2.0$ m, $\Delta t = 2$ s, $U_0 = 0.04$ m/s, $R = 80$ m, $M_0 = 1 \times 10^{-4}$, the Courant number $Co = u\Delta t/\Delta x \approx 0.1$, and the width of the slot is 16. According to the above parameter, the dimensionless number Pe is 800. The background velocity field for the present test is defined as

$$u = -U_0\pi\left(\frac{y}{L} - 0.5\right), \quad v = U_0\pi\left(\frac{x}{L} - 0.5\right). \tag{39}$$

Table II tabulates the relative errors E_ϕ from the present method in contrast to other solvers[36,61,65] at different Pe numbers. Generally, E_ϕ decreases with the reduction of mobility M_0 from 0.01 to 0.0001. Obviously, the relative error of the present method is smaller than the reference results from the lattice Boltzmann method (LBM) based on both the Cahn–Hilliard (CH) equation[61] and the Allen–Cahn (AC) equation under the same mesh resolution. In addition, the present method also exhibits higher accuracy than the hybrid spectral-difference LBM, which uses higher element order five and higher mesh resolution (6400 quadrilateral elements).[36] To further prove the high accuracy of the proposed method, we present the numerical error after a long time (ten cycles). Figure 3 shows the interface profile from the present method after one, two, four, eight, and ten cycles in comparison with the initial solution. By preserving the boundness of the phase variable solution through the more proper chemical potential, the proposed method achieves progress in both accuracy and stability, and the obtained results match well with the theoretical value at various times. From Table III, we can see the relative error E_ϕ from the present method and the approach in our recent publication[53] both grows with the increase in the number of cycles, but the value of E_ϕ is effectively reduced by more than 85% by the present method. In addition, as displayed in Fig. 3, the interface profile of the present method preserves the interface profile well in line with the analytical solution, and the relative error remains less than 1% even after ten rounds of rotation. Such an accuracy level for long-term computation has not been reported in the literature to the best of our knowledge. Moreover, the time consumption of present computation is also compared to our previous attempt,[53] and the present method saves 27.2% computation expense. Furthermore, we note that the proposed method can robustly provide convergent results for computations with large Pe numbers, while the model in Ref. 61 become unstable at Pe = 800 under same mesh resolution.

TABLE II. The relative errors E_ϕ of the present model and different models[36,61,65] for the problem of Zalesak's disk after one circle at Pe = 800.

	$U_0 = 0.04$ m/s			
M_0	Present	Wang *et al.*[65]	Liang *et al.*[61]	Ma *et al.*[36]
0.01	0.0126	0.0266	0.0485	/
0.001	0.0038	0.0409	0.0696	/
0.0001	0.0018	0.0491	/	0.0216

C. Single vortex flow

The single vortex flow[64,66–68] widely adopted to prove the convergence and interface capture accuracy of multiphase flows solvers. Driven by the time-dependent velocity field, the circular disk deforms to a slender filament in the first half of a period T, which spirals around the domain's center and exhibits strong nonlinear features in numerical simulation. At the second half of a period T, the circular disk will return to its initial position with shape unchanged in theory. Note that a longer period T give rise to more deformable interface, which renders the finial interface shape obtained hard to coincide with the initial interface shape. Figure 1(c) is a schematic diagram of the computational domain $\Omega = [0, L] \times [0, L]$. Mesh resolution of 161×161 (40 elements in both x- and y-directions) is used in this simulation. Initially, a circular disk with radius R is located at (x_0, y_0), and the unsteady velocity field is given as

$$\begin{aligned} u &= -U_0 \sin^2\frac{\pi x}{L}\sin\frac{\pi y}{L}\cos\frac{\pi y}{L}\cos\frac{\pi t}{T_f}, \\ v &= U_0 \sin\frac{\pi x}{L}\sin^2\frac{\pi y}{L}\cos\frac{\pi x}{L}\cos\frac{\pi t}{T_f}. \end{aligned} \tag{40}$$

where t is the time, $U_0 = 0.04$ m/s, $L = 200$ m, $R = $ L/5 m, $x_0 = 0.5L$, $y_0 = 0.75L$, $\varepsilon = 2.0$ m, the time step $\Delta t = 2$ s, $T_f = 6$ s which follows the case setup in Ref. 68.

Figure 4 shows the interface evolution during one cycle at Pe = 800. We observe that the disk is gradually drawn into a filament and spirals around the center of the vortex under the action of the underlying velocity field, and reach its maximum deformability at T/2. Later, it slowly returns to the initial state in the second half of the cycle. We can find that the numerical result based on present model accurately restore to the initial situation after one entire cycle as displayed in Fig. 4(f). For quantitative comparison with the reference solution,[68] the relative errors E_ϕ following Eq. (37) are listed in Table IV for different mobility parameters M_0. Again, the relative error of the present

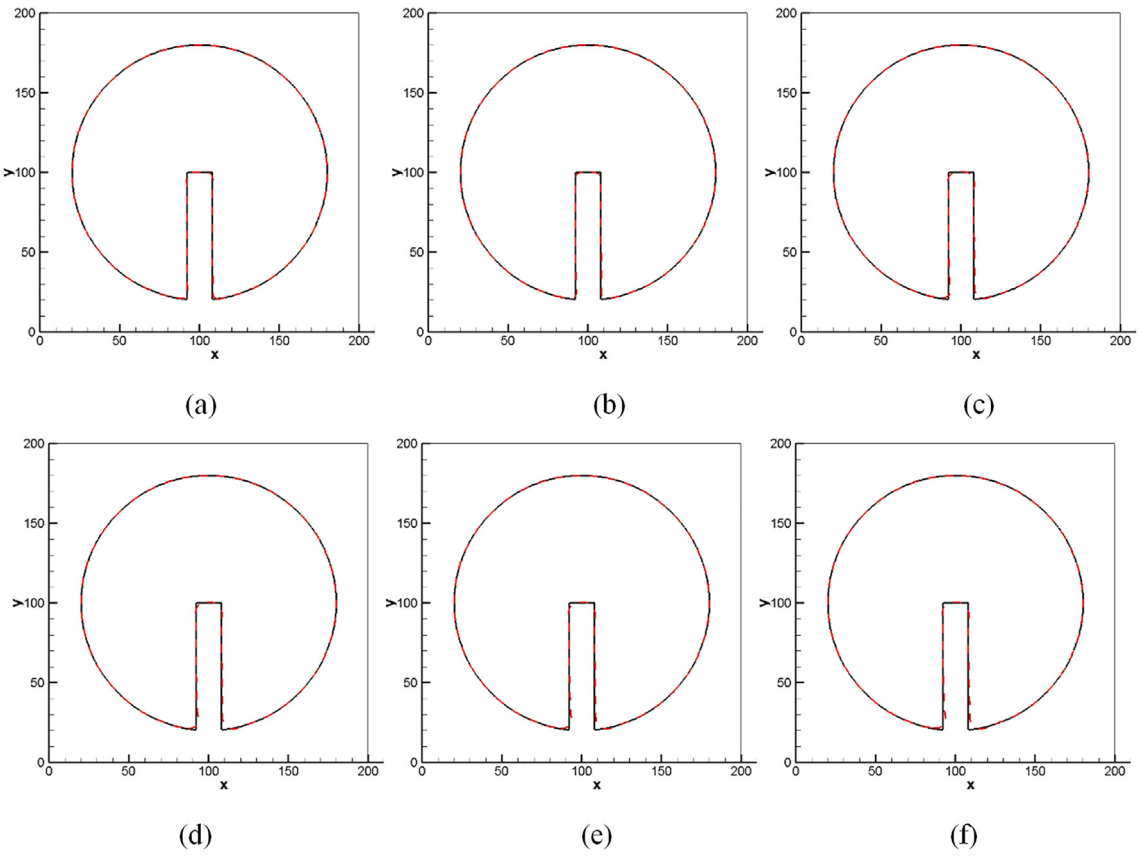

FIG. 3. The phase interface ($\phi = 0$) at different times when Pe = 800 (the black solid line is the initial value, and the red dashed line is the numerical solution): (a) t = T_f, (b) t = 5 T_f, (c) t = 10 T_f,(d) t = 6 T_f, (e) t = 8 T_f, and (f) t = 10 T_f.

method is much smaller than the result in the literature based on the CH equation[68] and also lower than results from the higher-order method in Ref. 53. Similar with the example above, comparison in the computation efficiency indicates that the present method saves 28.5% computation cost than our previous attempt in Ref. 53.

TABLE III. The relative errors E_ϕ of the present model and previous approach[53] for the problem of Zalesak's disk after multiple periods at Pe = 800.

Number of periods	Present method	Previous method[53]
1	0.0018	0.0141
2	0.0027	0.0220
3	0.0034	0.0278
4	0.0041	0.0324
5	0.0046	0.0362
6	0.0052	0.0394
7	0.0057	0.0422
8	0.0061	0.0447
9	0.0066	0.0469
10	0.0071	0.0489

IV. TESTS WITH COMPLEX CHANGE OF INTERFACE TOPOLOGY

In this section, we present two more numerical examples to assess the proposed method for more complex change of interface topology, its mobility parameter dependence, and versatility for problems with large fluid property contrast.

A. Two merging droplets

At first, the merging of two droplets is accounted. As displayed in Fig. 5, two droplets (density $\rho_1 = 10$ kg/m^3 and viscosity $\mu_1 = 0.1$ Pa s) with radius R_0 are initially placed at (−22.5 m, 0) and (22.5 m, 0) and dispersed in the second fluid (density $\rho_2 = 1$ kg/m^3 and viscosity $\mu_2 = 0.1$ Pa s), and the computational domain $\Omega = [0, L] \times [0, L]$ is covered by 2500 quadrilateral elements (50 elements in both x- and y-directions). When the initial gap d between two droplets is less than 2ε, coalescence of the two droplets occurs under the interfacial surface force.[69] The radii of the merged bubble R_T and the initial bubble R_0 follow the correlation $R_T = \sqrt{2}R_0$. The remaining parameters for the present test are $\varepsilon = 2.6$ m, $d = 2.5$ m, $\sigma = 0.01$ N/m, $M_0 = 0.0001$, $\Delta t = 1$ s, $L = 120$ m, and $R_0 = 20$ m. Figure 6 demonstrates the coalescence process of the two droplets, and the two droplets slowly come in contact at the beginning, then oscillate,

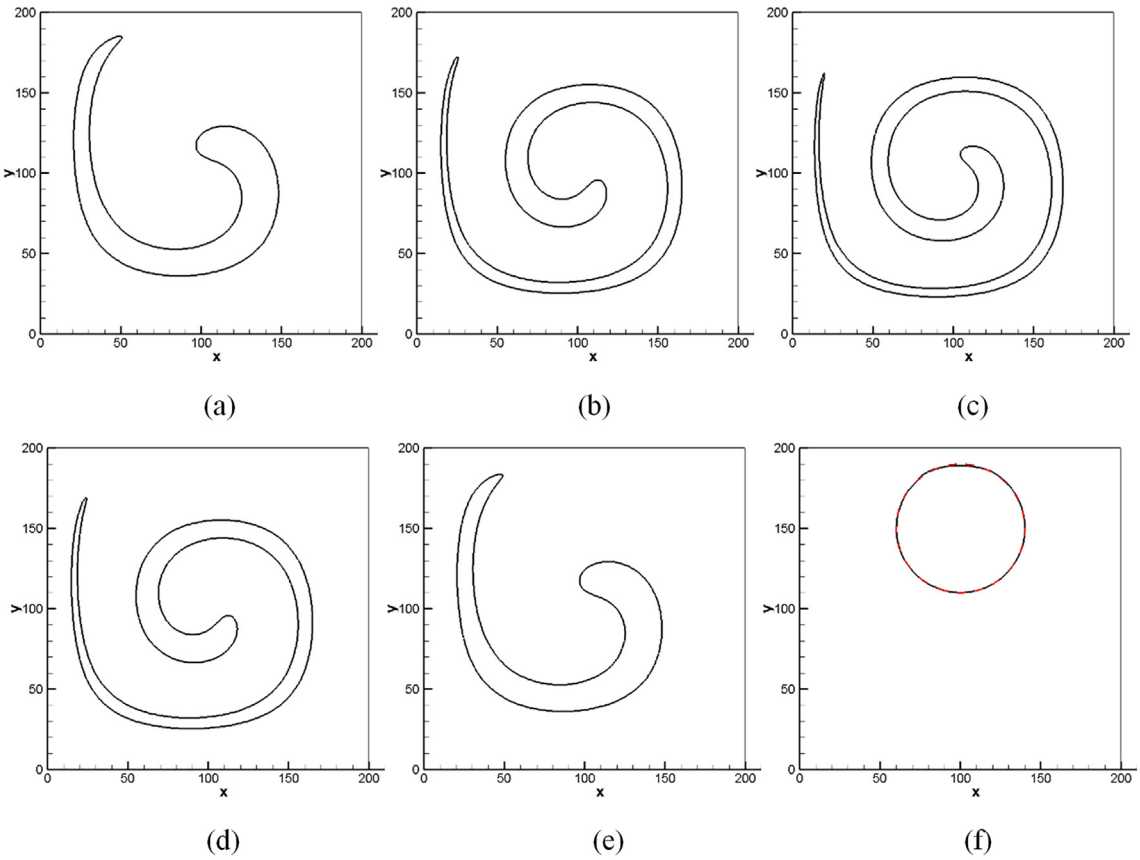

FIG. 4. The phase interface ($\phi = 0$) at different times at Pe = 800 (the black solid line is the numerical solution, and the red dashed line is the initial value): (a) t = $T_f/6$, (b) t = $T_f/3$, (c) t = $T_f/2$, (d) t = $2T_f/3$, (e) t = $5T_f/6$, and (f) t = T_f.

and finally form a larger stationary droplet. As in Fig. 6(f), the merged droplet become stable and its radius R_T accords well with the theoretical prediction, and there is not visual deviation between the initial value and numerical solution. Quantitatively, the relative error E_ϕ is 0.2% in the present work and 8.42% in Refs. 36 and 70, 3.81% in Refs. 71 and 72, and 1.39% in Ref. 41.

It is noted that the mobility dependence of the solution for the phase field model has hindered its further applications, and the choice of an appropriate mobility parameter remain an open question. Particularly, rich evidence has demonstrated that the coalescence process of the two droplets apparently depends on the mobility adopted. To provide deep insight on such issues, comparative studies are carried out based on five diverse mobility parameters, namely, $M_0 = 1 \times 10^{-4}$, 1×10^{-3}, 1×10^{-2}, 1×10^{-1}, and 1. The interface positions at t = 1000 steps computation are compared in Fig. 7. It is observed that the mobility will directly affect the merging speed of two droplets, and a larger mobility parameter aids in the coalescence significantly.

TABLE IV. The relative errors E_ϕ of the present model and literature[68] for the problem of single vortex flow.

	$U_0 = 0.04$ m/s		
M_0	Present	Xiao *et al.*[53]	Wang[68]
0.01	0.0301	0.0330	0.0447
0.001	0.0333	0.0409	0.0604
0.0001	0.0412	0.0468	0.1030

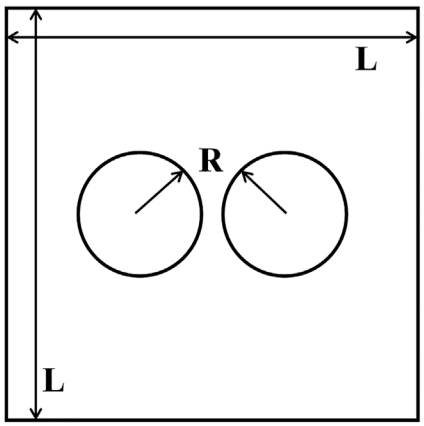

FIG. 5. Schematic diagram of two merging droplets.

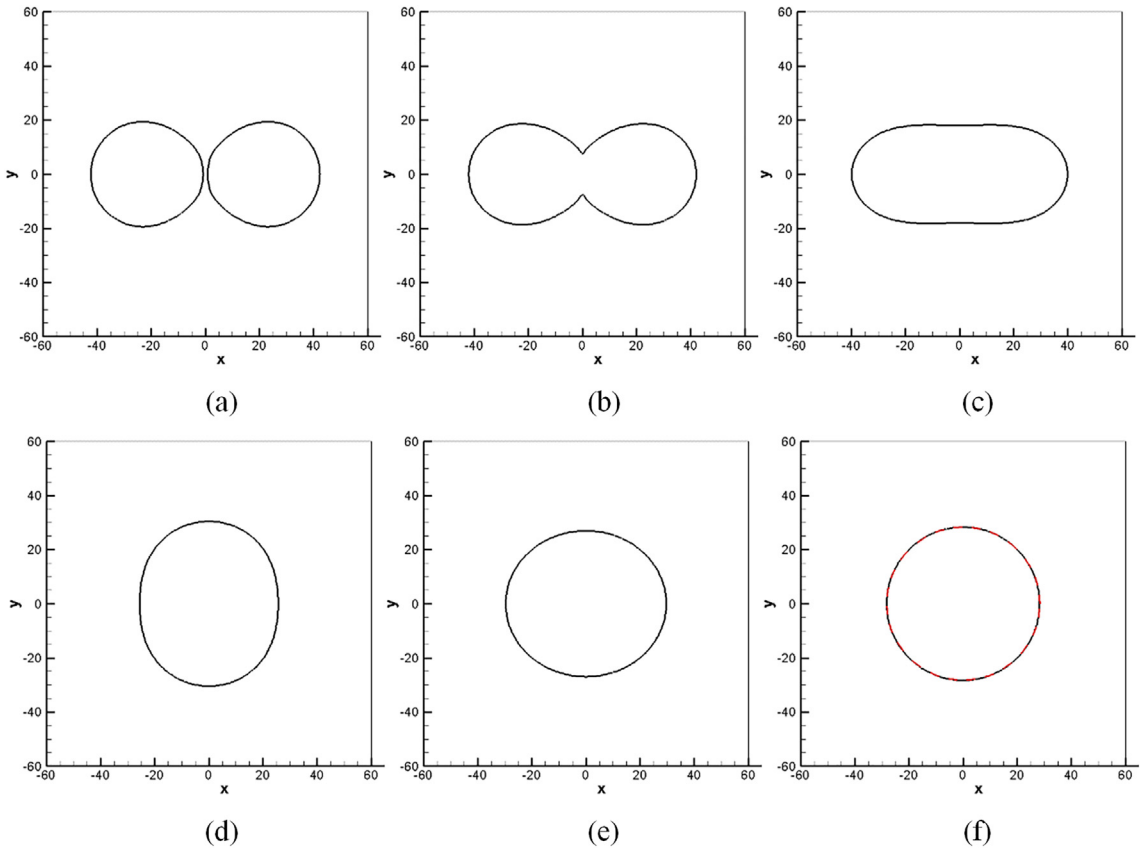

FIG. 6. The interface changes of bubble shape at different time steps (a) step =2000, (b) step = 3000, (c) step = 5000, (d) step = 10 000, (e) step = 20 000, and (f) step = 30 000, (red dotted line is the theoretical value; the black solid line is the numerical solution).

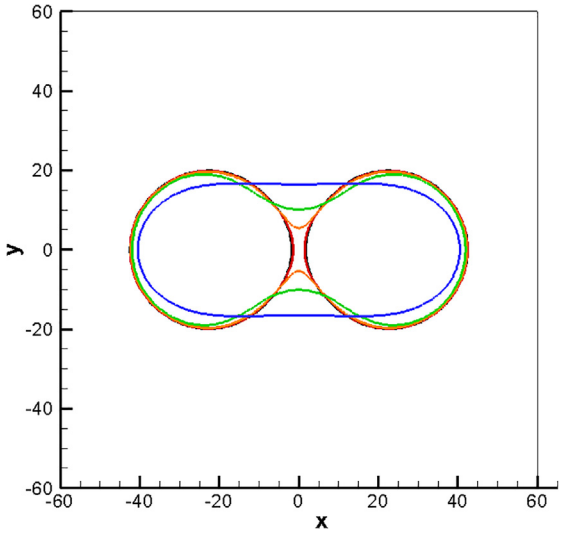

FIG. 7. The interface profile of droplets at t = 1000 steps with various mobilities (black solid line represents $M_0 = 1 \times 10^{-4}$; red solid line represents $M_0 = 1 \times 10^{-3}$; orange solid line represents $M_0 = 1 \times 10^{-2}$; green solid line represents $M_0 = 1 \times 10^{-1}$; and blue solid line represents $M_0 = 1$).

For $M_0 = 1$, the two droplets merge most rapidly, while no obvious difference is found between the cases of $M_0 = 1 \times 10^{-4}$ and $M_0 = 1 \times 10^{-3}$, and the corresponding merging speed is the slowest.

To gain deeper insight on the mobility's influence, we use the single stationary bubble to explore the dependence of motilities on the chemical potential. We place a single droplet in the center of the computational domain $\Omega = [0, L] \times [0, L]$, whose parameter setup is in line with above two merging droplets test. Here, we mainly concern the distribution of phase variable and chemical potential, as well as their relevance on the mobility parameter. Figure 8 presents the phase variable distribution at different mobilities ($M_0 = 1 \times 10^{-4}$, 1×10^{-3}, 1×10^{-2}, 1×10^{-1}, and 1). We observe that different mobilities have negligible impact on the distribution of phase variable, which is similar to the conclusion in Refs. 61 and 62. Moreover, Fig. 9 depicts the distribution of chemical potential for different mobilities considered and the distribution of phase variable at $M_0 = 1 \times 10^{-4}$ is also present for comparison. In contrast to the convergent distribution of phase variable, the solution for the chemical potential differs distinctly from each other for the cases with larger mobility parameters, i.e., $M_0 = 1 \times 10^{-2}$, 1×10^{-1}, and 1, while the convergent chemical potential profile is produced for the remaining two cases. In theory, the chemical potential takes effect in the vicinity of the interface, and ψ becomes to 0 in the place away from the interface. A larger mobility parameter ($M_0 = 1 \times 10^{-1}$ and 1)

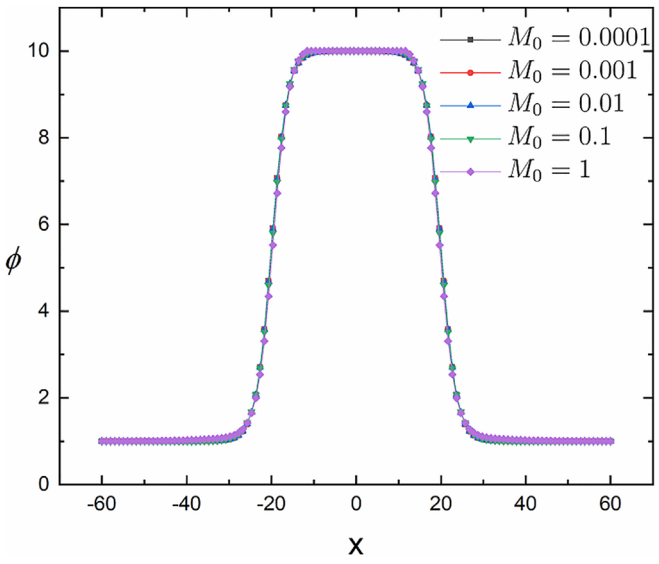

FIG. 8. The distribution of phase variable with different mobilities.

lead to much wider regions for the variation of the chemical potential than the interface area, which definitely favors the coalescence as in Fig. 7. In addition, in the case of $M_0 = 1 \times 10^{-2}$, the maximum value of the chemical potential does not reach the convergent results, thereby also gives rise to rapid merging procedure. While for the remaining cases with $M_0 = 1 \times 10^{-4}$ and 1×10^{-3}, the convergent chemical potential distribution corresponds the deterministic coalescence process as observed from Figs. 7 and 9. Therefore, we propose a fresh criterion for the choice of the mobility parameter based on the above observations that M_0 should be smaller than 1×10^{-3} to ensure a convergent solution for the chemical potential distribution, while its lower limit is referred to the scaling relation that the mobility should not be far smaller than $O(Cn^2)$,[42] which gives the complete criterion of the proposed phase-field-based method $O(Cn^2) \le M_0 \le 1 \times 10^{-3}$. In practical computations,

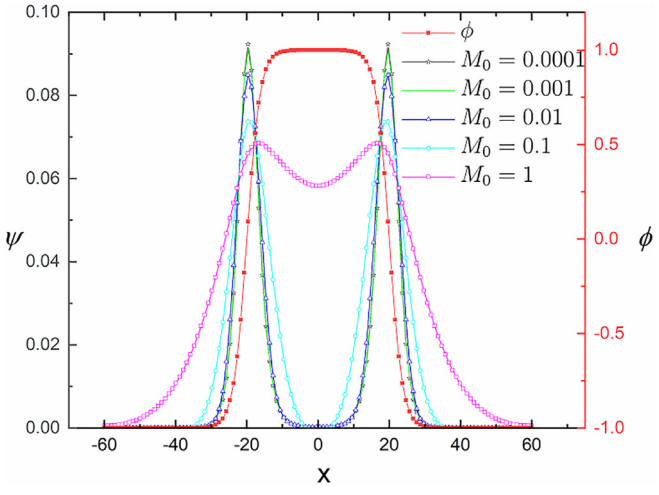

FIG. 9. The chemical potential distribution with different mobilities. Note that the distribution of phase variable at $M_0 = 1 \times 10^{-4}$ is included for comparison.

we cannot obtain convergent results for the cases with mobility parameter lower than this bound. We note that the validity of the proposed criterion can be supported by all the tests adopted in this work.

B. Bubble rising with large density contrast

In this subsection, we will further investigate the present method's robustness by simulating a rising bubble in water with the large density ratio (1000) and viscosity ratio (100). The domain $\Omega = L_2 \times L_1 = [0, 1] \times [0, 2]$ is filled with fluid 2 except for a dispersed circular bubble (fluid 1) as shown in Fig. 10. The initial bubble has a diameter of 0.5 with its center at (0.5, 0.5), which follows the problem setup in Ref. 73. The computational domain is covered by 4050 quadrilateral elements (45 elements in the x-direction and 90 elements in the y-direction). The no-slip boundary is imposed on the upper and lower boundaries, whereas the free slip boundary is applied on the left and right sides. The diameter of the bubble $D = 2R$ is chosen as the characteristic length of the problem, the dimensionless parameter Reynolds number Re and Eotvos number Eo are, respectively, defined as $\mathrm{Re} = \rho_2 g^{0.5} D^{1.5} / \mu_2$[73] and $\mathrm{Eo} = \rho_2 g D^2 / \sigma$, where the Eotvos number compares the gravity against the surface tension. The density and viscosity of fluids are denoted by ρ_1, ρ_2, μ_1, μ_2, respectively, and given in Table V. The interface thickness is set to be $\varepsilon = 0.01$ m. To quantitatively evaluate the results obtained, we use the following measured quantities same as in Refs. 53 and 73:

Center of mass:

$$y_c = \frac{\int_{\phi>0} y dx}{\int_{\phi>0} 1 dx}, \tag{41}$$

where y is the vertical coordinate value.

Rise velocity:

$$V_c = \frac{\int_{\phi>0} v dx}{\int_{\phi>0} 1 dx}, \tag{42}$$

where v is the y-component of the velocity $\mathbf{u}$.

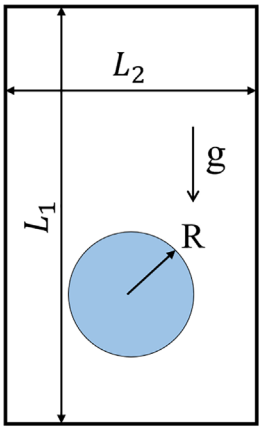

FIG. 10. Initial setup for the bubble rising problem.

TABLE V. The physical parameters and dimensionless values in the bubble rising test.

Case	*Eo*	*Re*	*D* (m)	G (m/s^2)	σ(N/m)	ρ_1(kg/m^3)	μ_1(Pa s)	ρ_2/ρ_1	μ_2/μ_1
A	10	35	0.5	0.98	24.5	100	1	10	10
B	125	35	0.5	0.98	1.96	1	0.1	1000	100

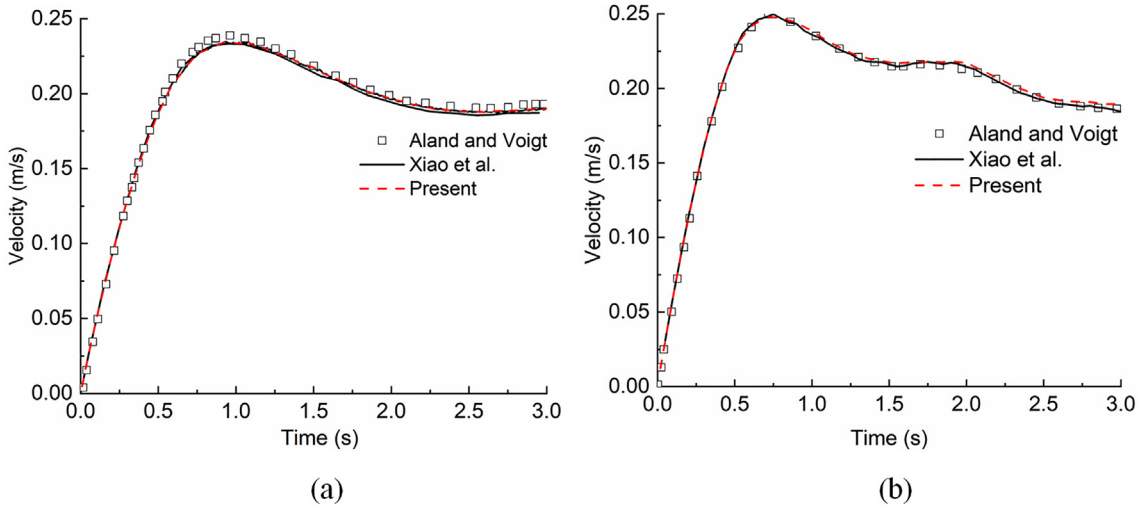

FIG. 11. Comparison of rising velocity V_c between benchmark solutions and numerical results of (a) case A and (b) case B.

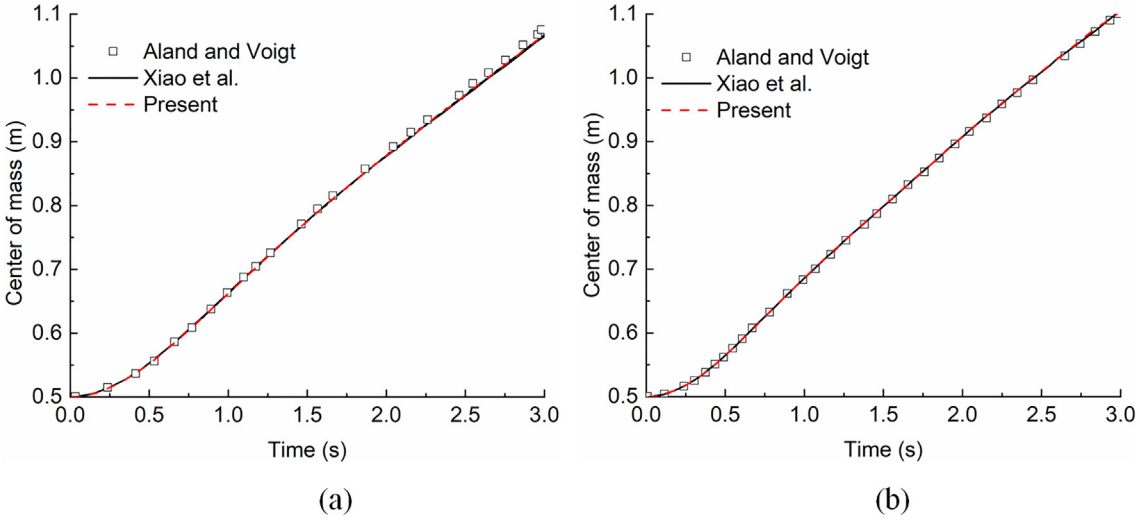

FIG. 12. Comparison of the mass center position y_c between benchmark solutions and numerical results of (a) case A and (b) case B.

The results from the present method match well with the reported data[53,74] as in Figs. 11–13. Figure 11 exhibits the comparison of rising velocity V_c between benchmark solutions and present results. In case A, the bubble rising velocity reaches the maximum at $t = 0.96$ and then gradually falls to a stable value; while in case B after reaching the maximum velocity, the velocity continues to decrease. This is due to the greater drag at the tail of the bubble during the rising, as shown in Fig. 14. Differing from the former Zalesak's disk rotation and single vortex flow examples, wherein only the CH equation is solved, the present test involves coupling between the N–S equations and the phase field equation; thus, the present method produces more pronounced savings in computation expense by 44.9%. Because the Jacobian matrix

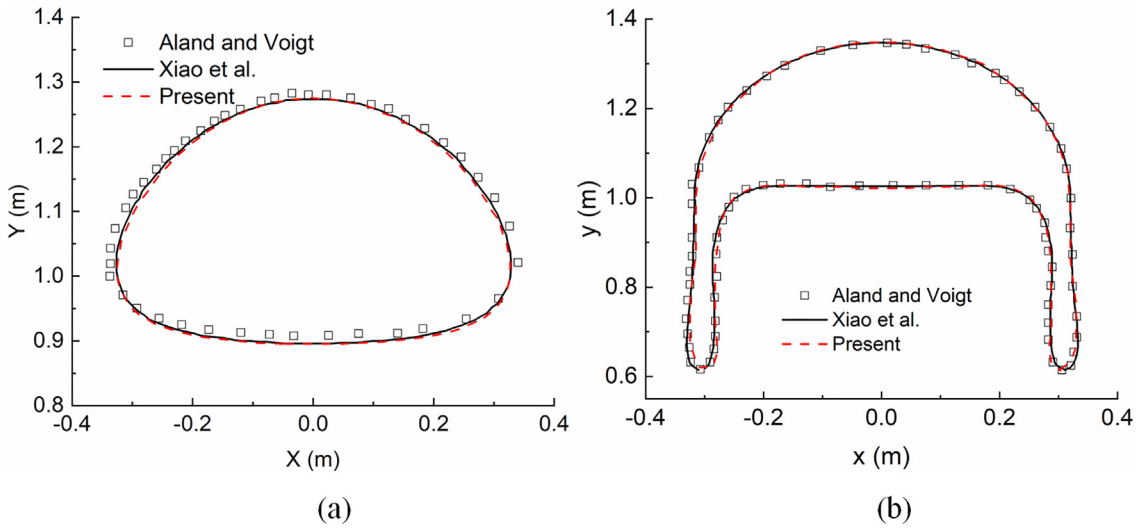

FIG. 13. Comparison the shape of bubble at time $t = 3$ between benchmark solutions and numerical results of (a) case A and (b) case B.

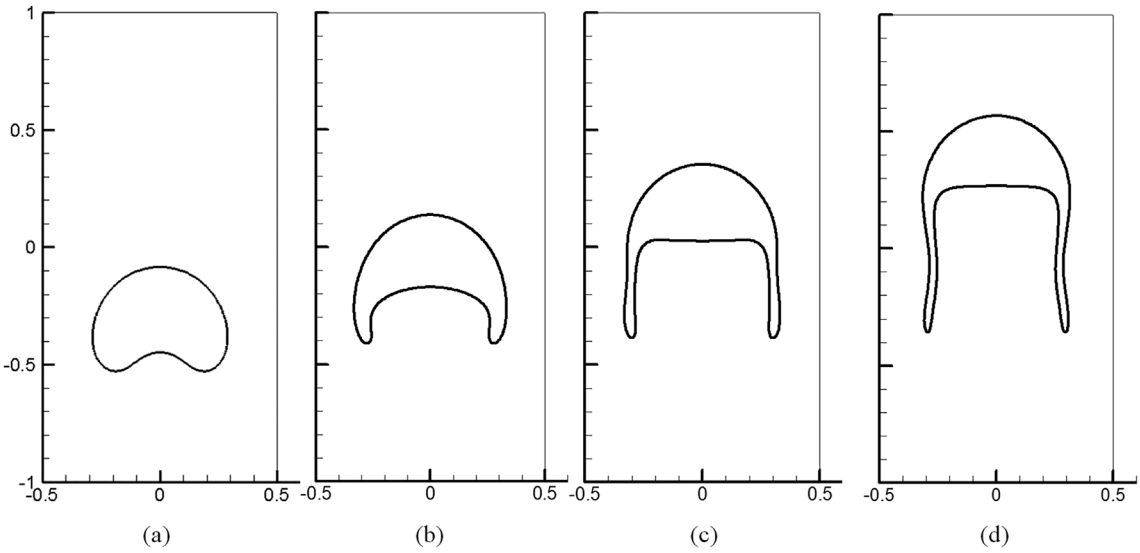

FIG. 14. The shape of bubbles for case B at different times: (a) $t = 1$, (b) $t = 2$, (c) $t = 3$, and (d) $t = 4$.

for the CH equation has the dimension of $[2N \times 2N]$, while the dimension of the coefficient matrix is $[N \times N]$ for the solution of pressure and each velocity component. Therefore, the constant coefficient matrix based discretization lead to nearly 27.2% savings of the computation expense for the phase field solution as in Sec. III B. While for the complete solutions for the two-phase flow as the example considered here, involving the velocity, pressure, and the phase field variable, the computation efficiency improvement is about 44.9%.

V. CONCLUSION

In this work, a phase-field-based spectral element approach is proposed for two-phase flows with large fluid property contrast. We propose to use the Newton–Raphson method to for the Cahn–Hilliard equation and adopt the time-stepping scheme for the Navier–Stokes equation. Accordingly, we construct three constant (time-independent) coefficient matrices for Cahn–Hilliard and Navier–Stokes equations. Such improvement in algorithm design avoids the coefficient matrix update for each iteration within every time step and, thus, gives rise to significant enhancement in computation efficiency over our previous high-accuracy attempt.[53] In addition, modification to the bulk free energy density is implemented to grant that the phase field solution is bounded, which benefits the interface capture accuracy greatly. After the spatial discretization within the spectral element method, we validate its robustness and versatility by numerical tests,

including diagonal motion of a circular interface, Zalesak's disk rotation, single vortex flow, two merging droplets, and bubbles merging. The proposed method enjoys high accuracy and stability in the tests of diagonal motion of a circular interface and Zalesak's disk rotation even for long-term computation, which outperforms the published efforts in the literature by far. From two merging droplets problem, we explore the mobility influence on the solution of the phase field model. We observe that the phase variable distribution for a single stationary droplet may be independent of the mobility adopted, but the chemical potential apparently diverges for various mobility parameters. Divergent chemical potential distribution definitely renders the droplet merging process dependent on mobility. Therefore, we propose a fresh criterion that an appropriate choice of the mobility parameter should ensure the convergence of the chemical potential. All the tests in this work support the validity of the proposed criterion. Moreover, the last test further proves the robustness of the proposed method for realistic two-phase flows with more complex interfacial dynamics and high fluid property contrast.

ACKNOWLEDGMENTS

This work was supported by the National Natural Science Foundation of China (Nos. 12172070 and 12102071), the Fundamental Research Funds for the Central Universities (No. 2021CDJQY-055), and the Science and Technology Research Program of Chongqing Municipal Education Commission (No. KJQN202100706).

AUTHOR DECLARATIONS

Conflict of Interest

The authors have no conflicts to disclose.

Author Contributions

Yao Xiao: Conceptualization (equal); Formal analysis (equal); Investigation (equal); Methodology (equal); Resources (equal); Software (equal); Validation (equal); Visualization (equal); Writing – original draft (equal); Writing – review and editing (equal). **Zhong Zeng:** Funding acquisition (lead); Project administration (equal); Supervision (lead); Writing – review and editing (supporting). **Liangqi Zhang:** Funding acquisition (lead); Project administration (equal); Supervision (supporting); Writing – review and editing (supporting). **Jingzhu Wang:** Methodology (supporting). **Yiwei Wang:** Methodology (equal). **Hao Liu:** Software (equal); Writing – review and editing (equal). **Chenguang Huang:** Investigation (equal).

DATA AVAILABILITY

The data that support the findings of this study are available from the corresponding author upon reasonable request.

REFERENCES

[1]Z. Luo, L. He, and B. Bai, "Deformation of spherical compound capsules in simple shear flow," J. Fluid Mech. **775**, 77 (2015).
[2]T.-V. Vu, T. V. Vu, and D. T. Bui, "Numerical study of deformation and breakup of a multi-core compound droplet in simple shear flow," Int. J. Heat Mass Transfer **131**, 1083 (2019).
[3]J. Wang, J. Liu, J. Han, and J. Guan, "Effects of complex internal structures on rheology of multiple emulsions particles in 2D from a boundary integral method," Phys. Rev. Lett. **110**, 066001 (2013).
[4]H. Hua, J. Shin, and J. Kim, "Dynamics of a compound droplet in shear flow," Int. J. Heat Fluid Flow **50**, 63 (2014).
[5]Y. Chen, X. Liu, and Y. Zhao, "Deformation dynamics of double emulsion droplet under shear," Appl. Phys. Lett. **106**, 141601 (2015).
[6]M. P. Borthakur, G. Biswas, and D. Bandyopadhyay, "Dynamics of deformation and pinch-off of a migrating compound droplet in a tube," Phys. Rev. E **97**, 043112 (2018).
[7]K. A. Smith, J. M. Ottino, and M. Olvera de la Cruz, "Encapsulated drop breakup in shear flow," Phys. Rev. Lett. **93**, 204501 (2004).
[8]Z. Che, Y. F. Yap, and T. Wang, "Flow structure of compound droplets moving in microchannels," Phys. Fluids **30**, 012114 (2018).
[9]S. Santra, S. Das, and S. Chakraborty, "Electrically modulated dynamics of a compound droplet in a confined microfluidic environment," J. Fluid Mech. **882**, A23 (2020).
[10]S. Santra, D. P. Panigrahi, S. Das, and S. Chakraborty, "Shape evolution of compound droplet in combined presence of electric field and extensional flow," Phys. Rev. Fluids **5**, 063602 (2020).
[11]X. Yang, A. J. James, J. Lowengrub, X. Zheng, and V. Cristini, "An adaptive coupled level-set/volume-of-fluid interface capturing method for unstructured triangular grids," J. Comput. Phys. **217**, 364 (2006).
[12]J. D. Van Der Waals, "The thermodynamic theory of capillarity under the hypothesis of a continuous variation of density," J. Stat. Phys. **20**, 200 (1979).
[13]J. W. Cahn, "Free energy of a nonuniform system. II. Thermodynamic basis," J. Chem. Phys. **30**, 1121 (1959).
[14]J. W. Cahn and J. E. Hilliard, "Free energy of a nonuniform system. I. Interfacial free energy," J. Chem. Phys. **28**, 258 (1958).
[15]J. W. Cahn and J. E. Hilliard, "Free energy of a nonuniform system. III. Nucleation in a two-component incompressible fluid," J. Chem. Phys. **31**, 688 (1959).
[16]L. Q. Chen and J. Shen, "Applications of semi-implicit Fourier-spectral method to phase field equations," Comput. Phys. Commun. **108**, 147 (1998).
[17]D. Jacqmin, "Contact-line dynamics of a diffuse fluid interface," J. Fluid Mech. **402**, 57 (2000).
[18]H. Ding, P. D. M. Spelt, and C. Shu, "Diffuse interface model for incompressible two-phase flows with large density ratios," J. Comput. Phys. **226**, 2078 (2007).
[19]P. Yue, J. J. Feng, C. Liu, and J. Shen, "A diffuse-interface method for simulating two-phase flows of complex fluids," J. Fluid Mech. **515**, 293 (2004).
[20]S. Dong, "Multiphase flows of N immiscible incompressible fluids: A reduction-consistent and thermodynamically-consistent formulation and associated algorithm," J. Comput. Phys. **361**, 1 (2018).
[21]Y. Hu, D. Li, X. Niu, and S. Shu, "A diffuse interface lattice Boltzmann model for thermocapillary flows with large density ratio and thermophysical parameters contrasts," Int. J. Heat Mass Transfer **138**, 809 (2019).
[22]H. H. Liu, L. Wu, Y. Ba, and G. Xi, "A lattice Boltzmann method for axisymmetric thermocapillary flows," Int. J. Heat Mass Transfer **104**, 337 (2017).
[23]Q. Li, Q. J. Kang, M. M. Francois, and A. J. Hu, "Lattice Boltzmann modeling of self-propelled Leidenfrost droplets on ratchet surfaces," Soft Matter **12**, 302 (2016).
[24]G. Duursma, R. Kennedy, K. Sefiane, and Y. Yu, "Leidenfrost droplets on microstructured surfaces," Heat Transfer Eng. **37**, 1190 (2016).
[25]Y. Wang, C. Shu, and L. M. Yang, "An improved multiphase lattice Boltzmann flux solver for three-dimensional flows with large density ratio and high Reynolds number," J. Comput. Phys. **302**, 41 (2015).
[26]T. Tao and Q. Zhonghua, "Efficient numerical methods for phase-field equations," Sci. Sin.-Math. **50**, 775 (2020).
[27]H. Shi and Y. Li, "Local discontinuous Galerkin methods with implicit-explicit multistep time-marching for solving the nonlinear Cahn-Hilliard equation," J. Comput. Phys. **394**, 719 (2019).
[28]Y. Cai and J. Shen, "Error estimates for a fully discretized scheme to a Cahn-Hilliard phase-field model for two-phase incompressible flows," Math. Comput. **87**, 2057 (2017).
[29]J. Shen and X. Yang, "Numerical approximations of Allen-Cahn and Cahn-Hilliard equations," Discrete Contin. Dyn. Syst. **28**, 1669 (2010).

[30]J. Shen and X. Yang, "A phase-field model and its numerical approximation for two-phase incompressible flows with different densities and viscosities," SIAM J. Sci. Comput. **32**, 1159 (2010).
[31]J. Shen and X. Yang, "Energy stable schemes for Cahn-Hilliard phase-field model of two-phase incompressible flows," Chin. Ann. Math. Ser. B **31**, 743 (2010).
[32]K. Park, M. Fernandino, and C. Dorao, "Numerical solution of incompressible Cahn-Hilliard and Navier-Stokes system with large density and viscosity ratio using the least-squares spectral element method," J. Fluid Flow Heat Mass Transfer **3**, 73–85 (2016).
[33]K. Park, M. Fernandino, C. A. Dorao, and M. Gerritsma, "The least-squares spectral element method for phase-field models for isothermal fluid mixture," Comput. Math. Appl. **74**, 1981 (2017).
[34]J. Manzanero, G. Rubio, D. A. Kopriva, E. Ferrer, and E. Valero, "A free–energy stable nodal discontinuous Galerkin approximation with summation-by-parts property for the Cahn–Hilliard equation," J. Comput. Phys. **403**, 109072 (2020).
[35]J. Manzanero, G. Rubio, D. A. Kopriva, E. Ferrer, and E. Valero, "Entropy–stable discontinuous Galerkin approximation with summation-by-parts property for the incompressible Navier–Stokes/Cahn–Hilliard system," J. Comput. Phys. **408**, 109363 (2020).
[36]C. Ma, J. Wu, and T. Zhang, "A high order spectral difference-based phase field lattice Boltzmann method for incompressible two-phase flows," Phys. Fluids **32**, 122113 (2020).
[37]S. Dong and J. Shen, "A time-stepping scheme involving constant coefficient matrices for phase-field simulations of two-phase incompressible flows with large density ratios," J. Comput. Phys. **231**, 5788 (2012).
[38]X. Zheng, H. Babaee, S. Dong, C. Chryssostomidis, and G. E. Karniadakis, "A phase-field method for 3D simulation of two-phase heat transfer," Int. J. Heat Mass Transfer **82**, 282 (2015).
[39]T. Inamuro, T. Ogata, S. Tajima, and N. Konishi, "A lattice Boltzmann method for incompressible two-phase flows with large density differences," J. Comput. Phys. **198**, 628 (2004).
[40]J. J. Huang, C. Shu, and Y. T. Chew, "Mobility-dependent bifurcations in capillarity-driven two-phase fluid systems by using a lattice Boltzmann phase-field model," Int. J. Numer. Methods Fluids **60**, 203 (2009).
[41]Z. Chen, C. Shu, D. Tan, X. D. Niu, and Q. Z. Li, "Simplified multiphase lattice Boltzmann method for simulating multiphase flows with large density ratios and complex interfaces," Phys. Rev. E **98**, 063314 (2018).
[42]D. Jacqmin, "Calculation of two-phase Navier–Stokes flows using phase-field modeling," J. Comput. Phys. **155**, 96 (1999).
[43]V. V. Khatavkar, P. D. Anderson, and H. E. H. Meijer, "On scaling of diffuse-interface models," Chem. Eng. Sci. **61**, 2364 (2006).
[44]F. Magaletti, F. Picano, M. Chinappi, L. Marino, and C. M. Casciola, "The sharp-interface limit of the Cahn–Hilliard/Navier–Stokes model for binary fluids," J. Fluid Mech. **714**, 95 (2013).
[45]D. Sharma, M. Coquerelle, A. Erriguible, and S. Amiroudine, "Adaptive interface thickness based mobility—Phase-field method for incompressible fluids," Int. J. Multiphase Flow **142**, 103687 (2021).
[46]H. Liu, A. J. Valocchi, Y. Zhang, and Q. Kang, "Lattice Boltzmann phase-field modeling of thermocapillary flows in a confined microchannel," J. Comput. Phys. **256**, 334 (2014).
[47]C. Liu and J. Shen, "A phase field model for the mixture of two incompressible fluids and its approximation by a Fourier-spectral method," Physica D **179**, 211 (2003).
[48]L. A. Caffarelli and N. E. Muler, "An L∞ bound for solutions of the Cahn-Hilliard equation," Arch. Ration. Mech. Anal. **133**, 129 (1995).
[49]D. J. Eyre, "Unconditionally gradient stable time marching the Cahn-Hilliard equation," MRS Online Proc. Lib. **529**, 39 (1998).
[50]J. Zhu, L. Q. Chen, J. Shen, and V. Tikare, "Coarsening kinetics from a variable-mobility Cahn-Hilliard equation: Application of a semi-implicit Fourier spectral method," Phys. Rev. E **60**, 3564 (1999).
[51]C. Xu and T. Tang, "Stability analysis of large time-stepping methods for epitaxial growth models," SIAM J. Numer. Anal. **44**, 1759 (2006).
[52]N. Condette, C. Melcher, and E. Süli, "Spectral approximation of pattern-forming nonlinear evolution equations with double-well potentials of quadratic growth," Math. Comput. **80**, 205 (2011).
[53]Y. Xiao, Z. Zeng, L. Zhang, J. Wang, Y. Wang, H. Liu, and C. Huang, "A spectral element-based phase field method for incompressible two-phase flows," Phys. Fluids **34**, 022114 (2022).
[54]H. Liu, A. J. Valocchi, Y. Zhang, and Q. Kang, "Phase-field-based lattice Boltzmann finite-difference model for simulating thermocapillary flows," Phys. Rev. E **87**, 013010 (2013).
[55]P. K. Kristensen and E. Martínez-Pañeda, "Phase field fracture modelling using quasi-Newton methods and a new adaptive step scheme," Theor. Appl. Fract. Mech. **107**, 102446 (2020).
[56]V. Badalassi, H. Ceniceros, and S. Banerjee, "Computation of multiphase systems with phase field models," J. Comput. Phys. **190**, 371 (2003).
[57]J. Shen and X. Yang, "An efficient moving mesh spectral method for the phase-field model of two-phase flows," J. Comput. Phys. **228**, 2978 (2009).
[58]S. B. Biner, *Programming Phase-Field Modeling* (SpringerLink, 2017).
[59]G. Karniadakis and S. Sherwin, *Spectral/hp Element Methods for Computational Fluid Dynamics* (Oxford University Press, Oxford, 2005).
[60]M. Geier, A. Fakhari, and T. Lee, "Conservative phase-field lattice Boltzmann model for interface tracking equation," Phys. Rev. E **91**, 063309 (2015).
[61]H. Liang, B. Shi, Z. Guo, and Z. Chai, "Phase-field-based multiple-relaxation-time lattice Boltzmann model for incompressible multiphase flows," Phys. Rev. E **89**, 053320 (2014).
[62]Y. Q. Zu and S. He, "Phase-field-based lattice Boltzmann model for incompressible binary fluid systems with density and viscosity contrasts," Phys. Rev. E **87**, 043301 (2013).
[63]S. T. Zalesak, "Fully multidimensional flux-corrected transport algorithms for fluids," J. Comput. Phys. **31**, 335 (1979).
[64]P.-H. Chiu and Y.-T. Lin, "A conservative phase field method for solving incompressible two-phase flows," J. Comput. Phys. **230**, 185 (2011).
[65]H. L. Wang, Z. H. Chai, B. C. Shi, and H. Liang, "Comparative study of the lattice Boltzmann models for Allen-Cahn and Cahn-Hilliard equations," Phys. Rev. E **94**, 033304 (2016).
[66]Z. Huang, G. Lin, and A. M. Ardekani, "Consistent, essentially conservative and balanced-force phase-field method to model incompressible two-phase flows," J. Comput. Phys. **406**, 109192 (2020).
[67]P. Frolkovič and C. Wehner, "Flux-based level set method on rectangular grids and computation of first arrival time functions," Comput. Visual. Sci. **12**, 297 (2009).
[68]H. Wang, "Phase-field lattice Boltzmann method for flow and heat transfer of multiphase fluid," Ph.D. dissertation (Huazhong University of Science and Technology, 2018).
[69]H. W. Zheng, C. Shu, and Y.-T. Chew, "A lattice Boltzmann model for multiphase flows with large density ratio," J. Comput. Phys. **218**, 353 (2006).
[70]T. Zhang, J. Wu, and X. Lin, "An interface-compressed diffuse interface method and its application for multiphase flows," Phys. Fluids **31**, 122102 (2019).
[71]Y. Wang, C. Shu, H. B. Huang, and C. J. Teo, "Multiphase lattice Boltzmann flux solver for incompressible multiphase flows with large density ratio," J. Comput. Phys. **280**, 404 (2015).
[72]Y. Wang, C. Shu, J. Y. Shao, J. Wu, and X. D. Niu, "A mass-conserved diffuse interface method and its application for incompressible multiphase flows with large density ratio," J. Comput. Phys. **290**, 336 (2015).
[73]S. Hysing, S. Turek, D. Kuzmin, N. Parolini, E. Burman, S. Ganesan, and L. Tobiska, "Quantitative benchmark computations of two-dimensional bubble dynamics," Int. J. Numer. Methods Fluids **60**, 1259 (2009).
[74]S. Aland and A. Voigt, "Benchmark computations of diffuse interface models for two-dimensional bubble dynamics," Int. J. Numer. Methods Fluids **69**, 747 (2012).